RSC Advances

PAPER

View Article Online
View Journal | View Issue

Cite this: *RSC Adv.*, 2026, **16**, 18802

1,2,4-Oxadiazolyl phenoxyacetic acid-modified algae-derived biochar for efficient *o*-nitrophenol removal: adsorption performance and mechanistic insights

Eman M. Abd El-Monaem, *[a] Ibtehal Mohamed,[b] Faisal Mohammed Alkahtani[c] and Mohammed Salah Ayoup[c]

In this study, a novel efficient adsorbent was engineered by supporting 2-(2-(3-phenyl-1,2,4-oxadiazol-5-yl)phenoxy)acetic acid (POPA) on algae-derived biochar (A-BC). The POPA@A-$BC_{0.5}$ composite was inspected using several characterization instruments to determine its chemical structure, surface charge, morphology, structural composition, and crystallographic phase. Furthermore, the adsorption capability of the POPA@A-$BC_{0.5}$ composite for *o*-nitrophenol (*o*-NP) was evaluated in an equilibrium batch adsorption experiment. The adsorption percentage of *o*-NP by POPA@A-$BC_{0.5}$ was 99.69% at pH 5 and a temperature of 20 °C. In addition, the *o*-NP adsorption reaction onto POPA@A-$BC_{0.5}$ reached equilibrium within 60 minutes. It was deduced from the isotherm analysis that *o*-NP adsorption onto POPA@A-$BC_{0.5}$ occurred *via* multilayer adsorption interactions, as it was best described by the Freundlich and Langmuir models. In parallel, the kinetic analysis indicated that the chemical interactions between *o*-NP and POPA@A-$BC_{0.5}$ governed the adsorption process because the pseudo-second order model fitted the experimental data. The performed mechanistic investigation suggested the participation of hydrogen bonds, electron donor–acceptor interactions, n → π* interactions, and π–π stacking in the adsorption of *o*-NP onto the POPA@A-$BC_{0.5}$ composite.

Received 15th February 2026
Accepted 25th March 2026

DOI: 10.1039/d6ra01348a

rsc.li/rsc-advances

1. Introduction

Water contamination is a multifaceted dilemma that requires urgent global action as it threatens the environment and human survival. Different pollutants negatively affect water quality, including heavy metals, residues from pharmaceutical and cosmetic industries, artificial dyes, and petroleum compounds.[1,2] Additionally, phenolic compounds are important industrial chemicals and are widely used in various industries, including petroleum refineries, explosives, plastics, pharmaceuticals, insecticides, petrochemicals, herbicides, and dyes.[3,4] As a consequence, the accumulation of phenolic compounds in water sources has exceeded acceptable limits, posing a serious threat to aquatic organisms, humans, plants, and animals.[5] The World Health Organization has emphasized the urgency of eliminating phenolic compounds from water bodies to limit their concentrations below 2 mg L^{-1} in drinking water.[6] Among phenolic compounds, *o*-nitrophenol (*o*-NP) is produced at a large scale, up to fifteen million pounds/year, since it is used for manufacturing *o*-aminophenol, *o*-nitroanisole, and other substances.[7,8] *o*-Nitrophenol is a water-soluble compound, affording an unpleasant odor and taste to water.[9] Moreover, *o*-NP can impact human health, as it causes mouth irritation, cyanosis, drowsiness, liver and kidney damage, and blurred vision.[10,11] To reduce the risks associated with *o*-NP, remediation methods such as biodegradation, catalytic reactions, filtration, adsorption, and electrochemical treatments have been developed.[11–13] Among these methods, adsorption is considered one of the most promising remediation approaches due to its cost-effectiveness, energy-saving nature, low toxicity, and simple operation.

Oxadiazole is a five-membered heterocyclic ring containing one oxygen atom and two nitrogen atoms in the ring system. Oxadiazole is one of the key nitrogen heterocycles that has shown promising results in various applications. Notably, the oxadiazole moiety has attracted research interest for the development of new compounds with potential therapeutic and environmental applications. This approach offers several advantages, including easy processing, low costs, short reaction times, and utility for library synthesis in industrial applications. The synthesis of the key carboxylic acid, 2-(2-(3-phenyl-1,2,4-oxadiazol-5-yl)phenoxy)acetic acid (POPA), has been previously

[a]*Advanced Technology Innovation, Borg El-Arab, Alexandria, Egypt. E-mail: emanabdelmonaem5925@yahoo.com*

[b]*Department of Chemistry, Faculty of Science, Alexandria University, Alexandria, Egypt*

[c]*Department of Chemistry, College of Science, King Faisal University, Al-Ahsa 31982, Saudi Arabia*

reported.[14] The application of POPA in combination with A-BC represents a novel protocol for removing nitrophenols from wastewater. The selective use of POPA with A-BC is mainly attributed to the presence of the carboxylic group, aromatic rings, and the 1,2,4-oxadiazole moiety, which can provide active sites for interaction with *o*-NP through hydrogen bonding, electron donor–acceptor interactions, and π–π stacking.

Carbonaceous biochar (BC) is a remarkable adsorbent that has attracted attention in the water treatment field due to its mechanical strength, low cost, high surface area, porous structure, excellent adsorption capacity, abundant oxygen-containing groups, and chemical stability.[15] In addition, biochar is considered a sustainable adsorbent because it can be produced from abundant biomass waste at a relatively low cost. Its porous carbon matrix and oxygen-containing surface groups provide diverse active sites for binding organic contaminants from water. Therefore, biochar-based materials have been widely investigated as promising adsorbents for environmental remediation applications.[16] Biochar is manufactured in the presence of limited oxygen by pyrolyzing various types of feedstock, such as agricultural waste, domestic waste, algae, poultry manure, and forestry waste.[17–19] The pyrolysis process of biomass can be classified into three types: slow pyrolysis at a temperature <300 °C, fast pyrolysis at a temperature exceeding 500 °C, and moderate pyrolysis at a temperature between 300 °C and 500 °C.[20] Notably, biochar has exhibited an outstanding capacity to adsorb inorganic and organic pollutants from polluted water bodies. The enhanced adsorbability of biochar can be attributed to its ability to attract the target contaminants *via* different chemical and physical pathways, including pore filling, π–π interactions, surface adsorption, hydrogen bonding, electrostatic interactions, Lewis acid–base interactions, ion exchange, and n → π interactions.[21] Therefore, combining POPA with algae-derived biochar is expected to provide a multifunctional adsorbent with enhanced affinity toward *o*-NP through the synergistic contribution of the porous structure and surface-active groups.

To the best of our knowledge, POPA has not been previously applied in wastewater remediation, and its combination with A-BC represents a novel approach for *o*-nitrophenol removal. In this approach, POPA was supported on algae-derived BC (A-BC) to fabricate a POPA@A-BC composite. The successful fabrication of the POPA@A-BC composite was verified using physicochemical characterization techniques, including zeta potential, scanning electron microscopy (SEM), X-ray diffraction (XRD), X-ray photoelectron spectroscopy (XPS), and Fourier transform infrared (FT-IR) spectroscopy analyses. The capability of the POPA@A-BC composite to adsorb *o*-NP and the best adsorption conditions were assessed *via* a series of batch experiments. Then, the experimental data from the *o*-NP adsorption reaction onto POPA@A-BC were analyzed using isotherm and kinetic models to investigate whether the controlling adsorption interactions were physical, chemical, or a combination of both. In addition, the mechanistic pathways of the adsorption reaction of *o*-NP onto the POPA@A-BC composite were proposed based on the XPS analysis of the composite before and after the reaction.

2. Experimental work

2.1. Synthesis of POPA

The synthetic pathway toward POPA started from the phenolic 1,2,4-oxadiazole **1**, which was treated with ethyl bromoacetate *via* an alkylation reaction, as depicted in Scheme 1, yielding the corresponding phenoxy acetate ester **2**. The saponification of **2** utilizing an aqueous NaOH/acidification protocol afforded the target acetic acid derivative (2-(2-(3-phenyl-1,2,4-oxadiazol-5-yl) phenoxy)acetic **3** (POPA). This compound was characterized using IR, HRMS, and NMR spectroscopy analyses, as reported previously.[14] The FT−IR spectrum of POPA showed a broad band at 3477 cm^{-1}, which corresponds to the OH of the carboxyl group, and strong bands at 1748 cm^{-1} (C=O) and 1601 cm^{-1} (C=N). All details of the chemical structure of POPA and the materials used during the fabrication steps are reported in Text S1 and S2.

2.2. Fabrication of A-BC

The A-BC was synthesized from green algae *via* moderate calcination, as follows: the green algae were washed sequentially with tap water, and then, it was purified with distilled H_2O. The algae were kept in an oven at 60 °C for one day to remove water and tune their texture to a crust-form, which facilitated its grinding. Next, the algae powder was transferred to a crucible and calcined for 3 hours at 500 °C. The obtained A-BC was collected and stored in a glass falcon until use in the fabrication of the POPA@A-BC composite.

2.3. Fabrication of the POPA@A-BC composite

The POPA@A-BC composite was produced using a post-synthesis approach.[22] A stoichiometric mass of POPA was dispersed in 15 mL of distilled water using sonication for 15 minutes. Then, A-BC was added to the POPA suspension and sonicated for 45 minutes. The POPA@A-BC composite was

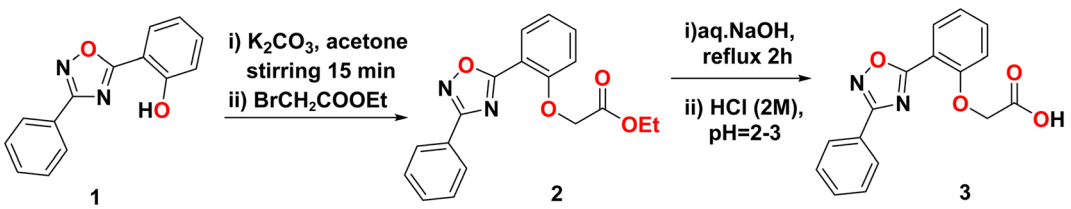

Scheme 1 Schematic of the fabrication steps of POPA.

collected by centrifugation and heated in an oven at 60 °C to evaporate water from the composite. The POPA@A-BC composite was prepared with three weight ratios of POPA to A-BC (1 : 1, 2 : 1, and 1 : 2), and they were labelled POPA@A-BC, POPA@A-BC$_{0.5}$, and POPA$_{0.5}$@A-BC, respectively.

2.4. Adsorption experiments

The key parameters of the *o*-NP adsorption onto the POPA@A-BC composite were investigated using several laboratory experiments, as follows: (1) the removal capabilities of POPA, A-BC, and POPA@A-BC composites toward *o*-NP were studied to select the best weight ratio of POPA to A-BC and to confirm the synergistic effect between them. (2) The adsorptive removal of *o*-NP by POPA@A-BC was studied at pH levels ranging from 3 to 11 to identify the most suitable pH medium. (3) The adsorption performance for *o*-NP was studied using four different dosages of the POPA@A-BC composite (5, 10, 15, and 20 mg) to determine the ideal dose. (4) The thermal state of the *o*-NP/POPA@A-BC system was monitored by inspecting the adsorption reaction at different temperatures ranging from 25 °C to 55 °C. (5) The maximum adsorption capacity of the POPA@A-BC composite toward *o*-NP and the equilibrium adsorption time were investigated by conducting the adsorption reaction at varying initial *o*-NP concentrations (C_i) in the range of 50–200 mg L^{-1} (6) the recycling test of the POPA@A-BC composite was executed for five *o*-NP adsorption cycles using NaOH as an eluent with a concentration of 1 M. The concentration of the unadsorbed *o*-NP (C_f) was measured after each experiment using a spectrophotometer. Notably, all adsorption experiments of *o*-NP on the POPA@A-BC composite were conducted in triplicate to ensure reproducibility, and the results are presented as mean ± standard deviation. No additional statistical significance test or mean separation analysis was performed in the present study. The removal percentage (R%) and adsorption capacity (q_t) of *o*-NP onto POPA@A-BC were calculated using the following equations:

$$R\% = \frac{C_0 - C_f}{C_0} \times 100, \quad (1)$$

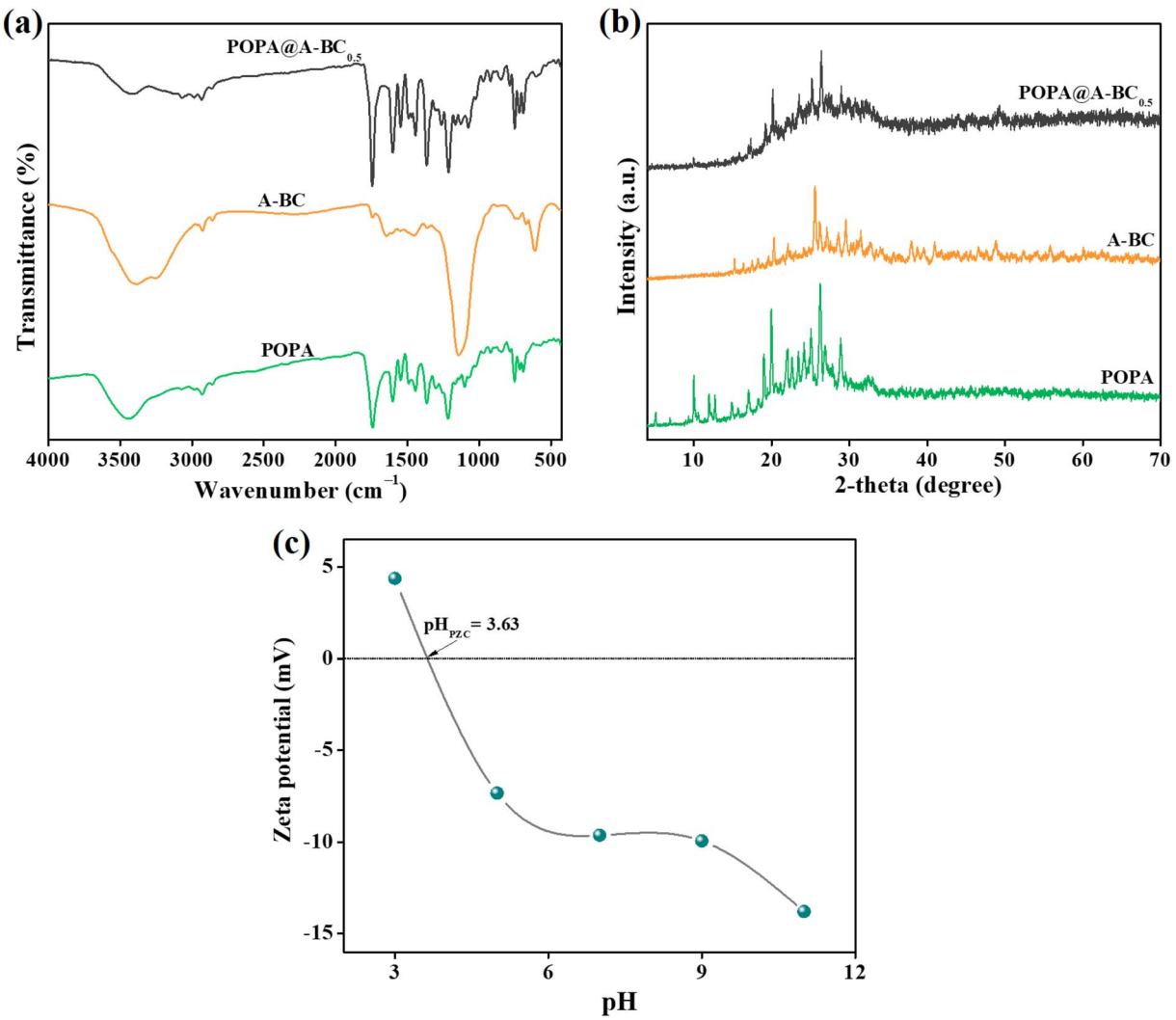

Fig. 1 (a) FTIR spectra and (b) XRD patterns of POPA, A-BC, and the POPA@A-BC$_{0.5}$ composite. (c) Zeta potential curve of the POPA@A-BC$_{0.5}$ composite.

$$q_t = \frac{(C_0 - C_f) \times V}{m}. \quad (2)$$

3. Results and discussion

3.1. Characterization of the POPA@A-BC composite

3.1.1. FT-IR. The chemical structures of POPA, A-BC, and the POPA@A-$BC_{0.5}$ composite were investigated using FT-IR analysis, as illustrated in Fig. 1a. The FT-IR spectrum of POPA showed a broad band at 3439 cm^{-1}, corresponding to the hydroxyl of the carboxylic group. Also, the FT-IR spectrum showed a strong band at 1742 cm^{-1}, corresponding to the carbonyl C=O of the carboxyl group, along with bands at 3071 cm^{-1} (Csp^2–H of aromatic C–H), 2983 cm^{-1} (Csp^3–H of aliphatic C–H), and 1602 cm^{-1} (C=C of the aromatic ring).[16] The FT-IR spectrum of A-BC showed broad bands at 3383 and 3251 cm^{-1}, corresponding to the hydroxyl group, and a very weak band at 1741 cm^{-1}, corresponding to the C=O of the carbonyl group. Also, the FT-IR spectrum showed a strong band at 1143 cm^{-1}, corresponding to the carbonyl C–O of the carboxyl group, along with bands at 3071 cm^{-1} (Csp^2–H of aromatic C–H), 2926 cm^{-1} (Csp^3–H of aliphatic C–H), and 1602 cm^{-1} (C=C of the aromatic ring). The FT-IR spectrum of the POPA@A-$BC_{0.5}$ composite showed a weak broad band at 3441 cm^{-1}, corresponding to the hydroxyl of the carboxylic group. Also, the FT-IR spectrum showed a strong band at 1743 cm^{-1}, corresponding to the carbonyl C=O of the carboxyl group, along with bands at 3068 cm^{-1} (Csp^2–H of aromatic C–H), 2983 cm^{-1} (Csp^3–H of aliphatic C–H), 1601 cm^{-1} (C=C of the aromatic ring), and 1126 cm^{-1} (C–O).

3.1.2. XRD. The crystallographic profiles of POPA, A-BC, and the POPA@A-$BC_{0.5}$ composite were determined by XRD analysis, as shown in Fig. 1b. In the XRD pattern of POPA, the diffraction peaks between $2\theta = 15°$ and 30° confirm the ordered molecular domain. In addition, the sharp peaks of POPA suggest its semi-crystalline structure, which can be due to the π–π stacking in the aromatic group-based conjugated system of the POPA backbone.[23] The crystallographic pattern of A-BC demonstrates the characteristic peak of graphitic carbon at $2\theta = 26.1°$, which is accompanied by the (002) plane.[24] The high crystallinity of the graphite peak is most likely due to the crystalline ordering and the existence of inorganic minerals of algae (*viz.*, Si, Ca, and Mg). The peaks related to MgO appear at $2\theta =$ 37.09°, 43.86°, and 60.04°.[25] The calcite peaks emerge at $2\theta =$ 30.47°, 48.72°, and 40.92°, while the peak related to quartz emerges at 20.27°.[26,27] The XRD profile of the POPA@A-$BC_{0.5}$ composite exhibits the attenuation of the characteristic peaks of the parent components, particularly A-BC because the concentration of POPA in the composite is double the concentration of A-BC. In addition, the POPA particles present on the A-BC surface prevent the diffraction beam from reaching the A-BC crystals. Notably, there is no new peak in the crystallographic pattern of the POPA@A-$BC_{0.5}$ composite, confirming the physical bonding between POPA and A-BC as the post-synthesis approach was used to manufacturing the composite.

3.1.3. Zeta potential. The change in the surface charge of the POPA@A-$BC_{0.5}$ composite with an increase in the pH of the media from 3 to 11 was monitored by zeta potential analysis, as shown in Fig. 1c. The zeta potential curve of the POPA@A-$BC_{0.5}$ composite shows that its zero-charge point (pH_{pzc}) is 3.63. The functional groups of the POPA@A-$BC_{0.5}$ composite (*viz.*, COOH and OH) protonate at pH values lower than 3.63 because of the abundant H^+ ions. This protonation gives rise to a net positive surface charge on the POPA@A-$BC_{0.5}$ surface, making the composite more likely to adsorb anionic adsorbates in highly acidic media *via* coulombic attraction forces. Conversely, as the pH increases, the functional groups of the POPA@A-$BC_{0.5}$ composite gradually deprotonate, reducing the positive surface charges and shifting the zeta potential toward negative values at pH levels above 3.63. At this point, the POPA@A-$BC_{0.5}$ composite is suitable for adsorbing cationic adsorbates due to the coulombic attraction forces generated between them.

3.1.4. XPS. Fig. 2a–d presents the elemental composition of the POPA@A-$BC_{0.5}$ composite based on the XPS spectrum. The wide scan spectrum illustrates the peaks for carbon, oxygen, and nitrogen at 285.38, 533.30, and 399.87 eV, with atomic percentages of 70.52%, 22.24%, and 4.99%, respectively. In addition, the binding peak of magnesium is observed at 1305.30 eV, which may be attributed to the thermal stability of the inorganic minerals in algae, such as Mg. Therefore, the inorganic minerals remain as a solid residue in BC. Conversely, the organic components in the algae feedstock, such as carbohydrates, lipids, and proteins, decompose during the pyrolysis process. The XPS spectrum of C 1s reveals the carbon-based functional groups of the POPA@A-$BC_{0.5}$ composite, such as C–C, C–O, O–C=O, and N=C–N, and their peaks appear at 284.76, 286.47, 287.52, and 289.21 eV, respectively. Furthermore, the atomic percentages of C–C, C–O, O–C=O, and N=C–N are found to be 64.00%, 20.92%, 9.58%, and 5.50%, respectively. The O 1s spectrum shows the C=O and C–OH peaks at 531.34 and 533.05 eV, with atomic percentages of 42.12% and 57.88%, respectively. The N 1s spectrum displays two peaks at 398.83 and 400.21 eV, which are associated with N=C–N and C–N, and their atomic percentages are 83.65% and 16.35%, respectively.

3.1.5. SEM and SEM-EDX. Fig. 3a–d demonstrates the morphologies of A-BC, POPA, and the POPA@A-$BC_{0.5}$ composite detected *via* SEM analysis. The SEM image of A-BC shows a porous carbon framework with a rough surface, providing many anchoring sites for supporting active species. In POPA, the particles appear as rod-like microcrystals with a smooth surface. Furthermore, the POPA microcrystals are almost uniform and well-defined, reflecting their high crystallinity. The SEM image of the POPA@A-$BC_{0.5}$ composite demonstrates the distribution of the POPA crystals on the surface and within the pores of A-BC. Obviously, the porous carbon framework of A-BC improves the dispersity of POPA crystals and limits their agglomeration, resulting in the formation of a composite with enhanced homogeneity. The SEM-EDX analysis of A-BC (Fig. 3e) shows that it mainly consists of carbon and oxygen, with mass percentages of 49.09% and 35.79%, respectively. In addition, some trace elements are detected in the SEM-EDX spectrum of

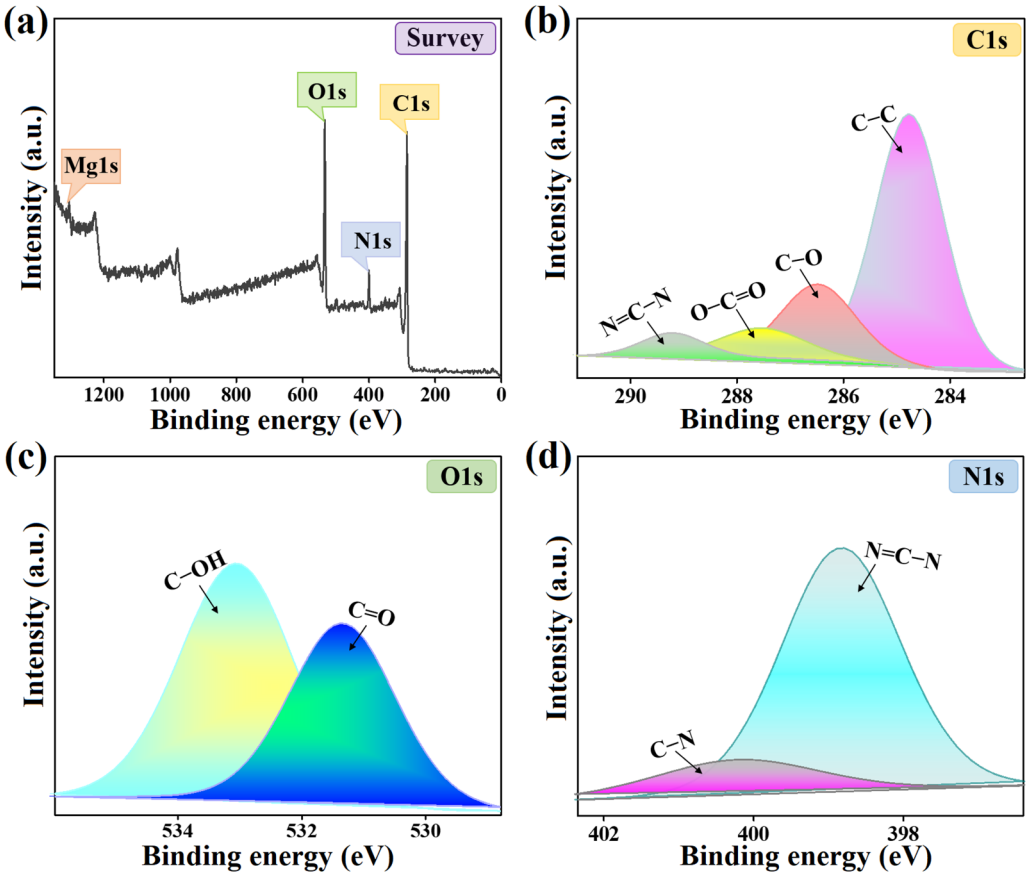

Fig. 2 XPS analysis of the POPA@A-$BC_{0.5}$ composite: (a) wide scan, (b) C 1s, (c) O 1s, and (d) N 1s spectra.

A-BC, including silicon, calcium, sodium, magnesium, sulfur, and chloride, which may originate from the algae. The SEM-EDX analysis of the POPA@A-$BC_{0.5}$ composite reveals a new nitrogen peak (12.97%), attributed to POPA, thereby confirming the successful incorporation of POPA onto A-BC (Fig. 3f). Furthermore, the carbon content increases to 56.37% and the oxygen content decreases to 29.80% after modification. This observation is consistent with the incorporation of POPA, which is relatively rich in carbon. Meanwhile, the decrease in the oxygen content may be attributed to the change in the relative surface elemental composition after POPA loading. These findings confirm the successful loading of POPA onto the A-BC surface.

3.2. Identification of the key parameters of *o*-NP adsorption

3.2.1. Investigating the optimal POPA : A-BC ratio. A comparison experiment was conducted between the removal capabilities of POPA, A-BC, POPA@A-BC, POPA@A-$BC_{0.5}$, and $POPA_{0.5}$@A-BC toward *o*-NP under the same adsorption conditions, as illustrated in Fig. 4a. The adsorption percentage and adsorption capacities of POPA and A-BC were 72.67% and 81.06 mg g^{-1} and 57.56% and 70.58 mg g^{-1}, respectively. In addition, the adsorption efficacies of *o*-NP onto POPA@A-BC, $POPA_{0.5}$@A-BC, and POPA@A-$BC_{0.5}$ were 88.78, 86.35, and 93.97 mg g^{-1}, while their adsorption percentages were 83.82%, 80.31%, and 91.35%, respectively. These findings confirmed the synergistic effect between POPA and A-BC, which created an efficient adsorbent with an outstanding removal capacity toward the noxious *o*-NP molecule. Because the adsorption of *o*-NP does not depend on coulombic attraction forces, like most of the adsorbates, it needs an adsorbent rich with active groups to attract *o*-NP *via* numerous pathways. Consequently, coupling POPA and A-BC provides excess aromatic rings that can interact with *o*-NP *via* π–π stacking. In addition, the composite possesses oxygenated functional groups that can share electrons to bond with *o*-NP *via* n–π interactions, electron donor–acceptor interactions, and hydrogen bonding. Finally, POPA@A-$BC_{0.5}$ exhibited the highest adsorption capacity toward *o*-NP, so it was selected for subsequent batch adsorption experiments.

3.2.2. Investigating the optimal pH medium. Fig. 4b depicts the variation in the adsorption efficiency of *o*-NP onto the POPA@A-$BC_{0.5}$ composite with an increase in the pH from 3 to 11. The experimental results demonstrated that the adsorption percentage and adsorption capacity of *o*-NP at pH 3 were 68.59% and 78.10 mg g^{-1}, respectively. Then, an increase in the pH to 5 increased the adsorption percentage and adsorption capacity of *o*-NP to 91.35% and 93.96 mg g^{-1}, respectively. Furthermore, increasing the pH to neutral and alkaline gradually decreased the adsorption percentage and adsorption efficiency of o-NP, which were 52.81% and 67.09 mg g^{-1} at pH 11, respectively. Meanwhile, *o*-NP exists in the molecular form until pH 7.2, and it begins to ionize at pH > 7.2 and carries a net

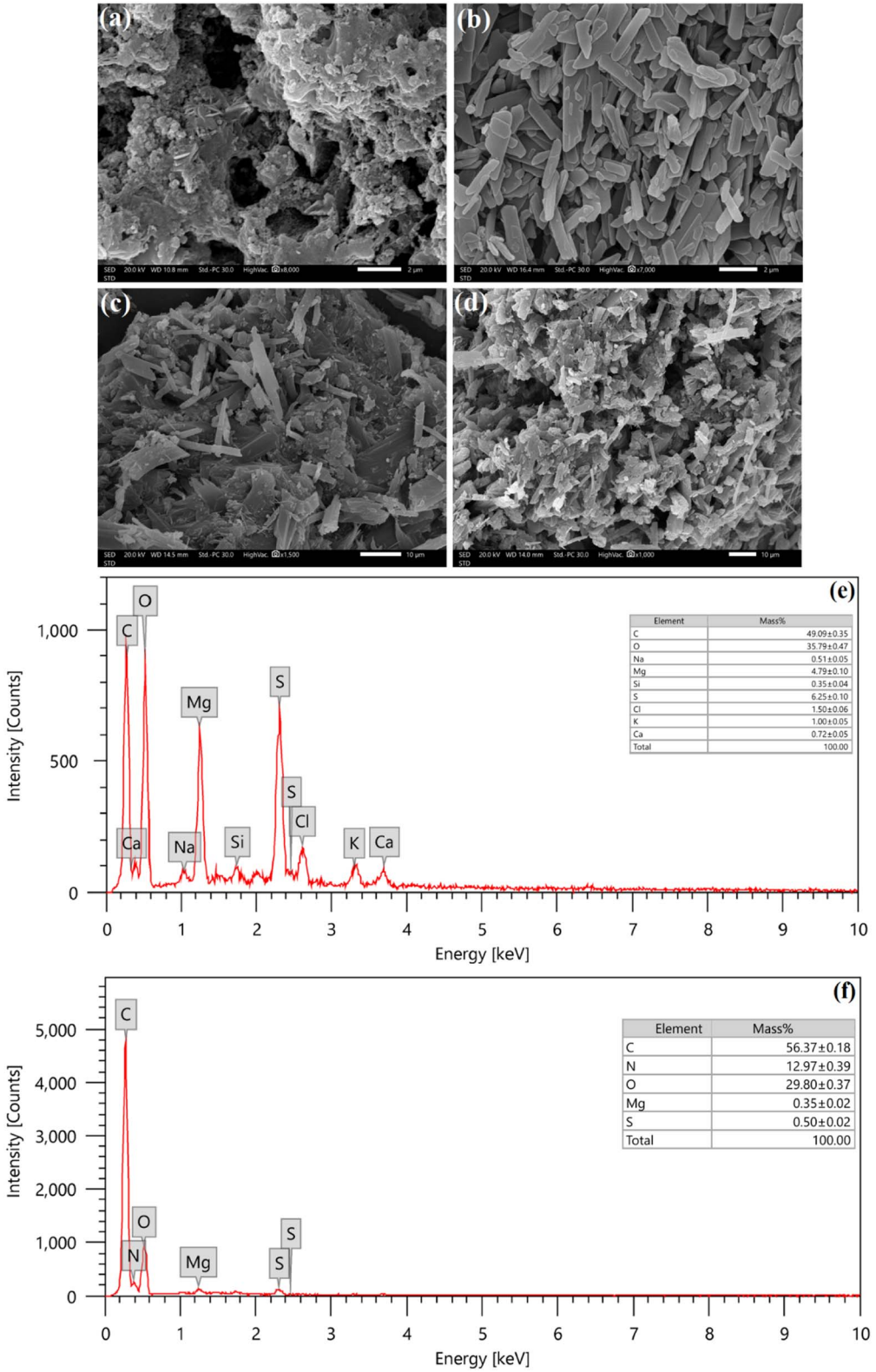

Fig. 3 SEM images of (a) A-BC, (b) POPA, and (c and d) the POPA@A-$BC_{0.5}$ composite. SEM-EDX spectra of (e) A-BC and (f) the POPA@A-$BC_{0.5}$ composite.

negative charge.[28] The experimental observations may be explained as follows: at pH = 3, the functional groups of POPA@A-$BC_{0.5}$ are protonated; consequently, the composite can interact with *o*-NP *via* π–π stacking and hydrogen bonding. Further, the abundant H^+ ions in the highly acidic medium increase the competition, which hinders the adsorption of *o*-NP

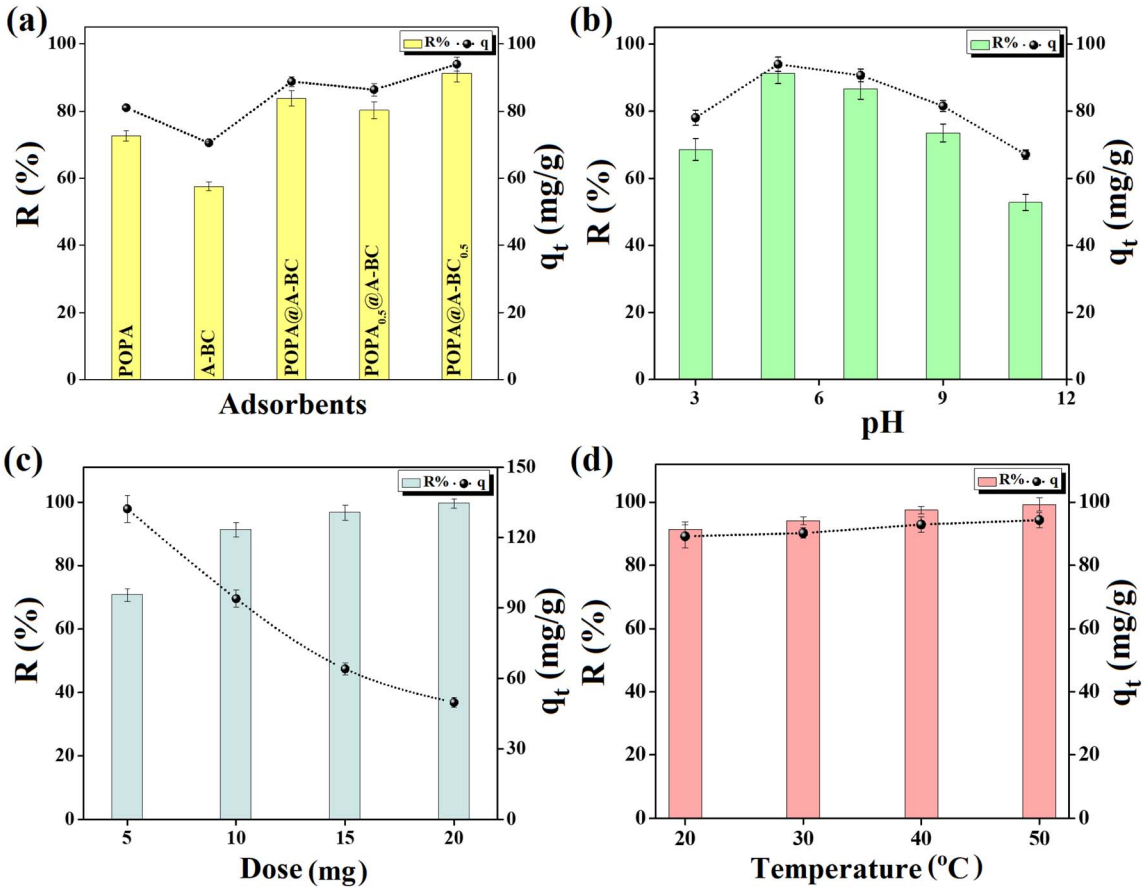

Fig. 4 Recorded experimental results of the (a) comparison test (C_o = 50 mg L^{-1}, m = 10 mg, V = 20 mL, T = 20 °C, and pH = 5), (b) investigation on the impact of pH (pH = 3–11, C_o = 50 mg L^{-1}, m = 10 mg, V = 20 mL, and T = 20 °C), (c) investigation on the optimal POPA@A-$BC_{0.5}$ dosage (m = 5–20 mg, C_o = 50 mg L^{-1}, V = 20 mL, T = 20 °C, and pH = 5), and (d) investigation on the thermodynamics behavior of the adsorption system (T = 20–50 °C, C_o = 50 mg L^{-1}, m = 10 mg, V = 20 mL, and pH = 5).

onto the POPA@A-$BC_{0.5}$ composite. At pH = 5, the POPA@A-$BC_{0.5}$ composite is still protonated in the presence of available oxygenated groups and a decrease in the H^+ concentration in the adsorption system. Therefore, the interactions between POPA@A-$BC_{0.5}$ and *o*-NP become stronger, and different adsorption pathways can contribute to the adsorption process, such as π–π stacking, electron donor–acceptor interactions, n–π interactions, and hydrogen bonds. Then, when the pH is elevated to pH = 7, *o*-NP is partially deionized, while the POPA@A-$BC_{0.5}$ composite carries a negative charge, resulting in the generation of coulombic repulsion forces and a decrease in the adsorption capability. At pH ≥ 9, *o*-NP is fully ionized, converting it to an anionic molecule and strengthening the coulombic repulsion forces between the POPA@A-$BC_{0.5}$ composite and *o*-NP. In parallel, the ample OH^- ions increase the competition and hinder the adsorption of *o*-NP onto the POPA@A-$BC_{0.5}$ composite.

3.2.3. Investigating the optimal adsorbent dosage. One of the most significant advantages of the selected adsorbent for water remediation is that it exhibits high adsorbability at a low adsorbent dose. Consequently, the *o*-NP adsorption process was performed with varied dosages of the POPA@A-$BC_{0.5}$ composite to determine the equilibrium dose. Obviously, the adsorption percentage of *o*-NP increased from 70.70% to 91.35% when the POPA@A-$BC_{0.5}$ dosage was doubled from 5 to 10 mg, as shown in Fig. 4c. This adsorption performance may be due to an increase in the available surface area and binding sites with increasing POPA@A-$BC_{0.5}$ dosage. Nevertheless, raising the POPA@A-$BC_{0.5}$ dose to 15 and 20 mg resulted in an insignificant improvement in the adsorption percentage of *o*-NP by 5.45% and 8.28%, respectively. On the other side, an increase in the POPA@A-$BC_{0.5}$ dosage diminished the adsorption capacity of *o*-NP from 132.28 to 49.79 mg g^{-1}. This result can be attributed to the lower *o*-NP concentration compared with the available adsorption sites, which increases the number of unreacted binding sites on the POPA@A-$BC_{0.5}$ composite.[29]

3.2.4. Investigating the thermal behavior. The thermodynamics of *o*-NP adsorption onto the POPA@A-$BC_{0.5}$ composite was scrutinized at process temperatures between 20 °C and 50 °C. As shown in Fig. 4d, the thermodynamics of the *o*-NP–POPA@A-$BC_{0.5}$ adsorption system is endothermic because the adsorption percentage of *o*-NP reaches almost 100% and the adsorption capacity is 99.37 mg g^{-1} when the temperature increases to 50 °C. This observation is most likely due to the enhancement in the molecular mobility of *o*-NP and the decrease in the diffusion resistance at higher reaction

temperatures, which facilitates the transport of *o*-NP to the adsorption sites of the POPA@A-$BC_{0.5}$ composite.[30] Therefore, higher thermal energy favors the interactions between *o*-NP and the POPA@A-$BC_{0.5}$ composite.

3.3. Kinetics and isotherm studies

To determine the highest adsorption percentage and maximum adsorption capacity of the POPA@A-$BC_{0.5}$ composite toward *o*-NP, the adsorption reaction was performed by varying the initial *o*-NP concentration. As shown in Fig. 5a, the adsorption percentage of *o*-NP increased rapidly with time, proving the presence of ample vacant adsorption sites on the POPA@A-$BC_{0.5}$ surface. After 60 minutes, the adsorption capacity of *o*-NP increased slowly, indicating that the adsorption reaction had reached equilibrium. In addition, the adsorption percentage of *o*-NP declined from 99.69% to 67.87% with increasing *o*-NP concentration from 50 to 200 mg L^{-1} due to a decrease in the number of vacant active sites on the POPA@A-$BC_{0.5}$ composite at high *o*-NP concentrations. Additionally, the adsorption capacity of the POPA@A-$BC_{0.5}$ composite for *o*-NP increased from 99.78 to 294.60 mg g^{-1} with increasing initial concentration, as shown in Fig. 5b. This result is most likely because the strengthened driving force at higher concentrations of *o*-NP surpasses the resistance of mass transfer to the POPA@A-$BC_{0.5}$ surface.[31,32] Therefore, the adsorption percentage of *o*-NP by POPA@A-$BC_{0.5}$ was 99.69%, the maximal capacity of the adsorbed *o*-NP molecules was 294.60 mg g^{-1}, and the equilibrium time was found to be 60 minutes.

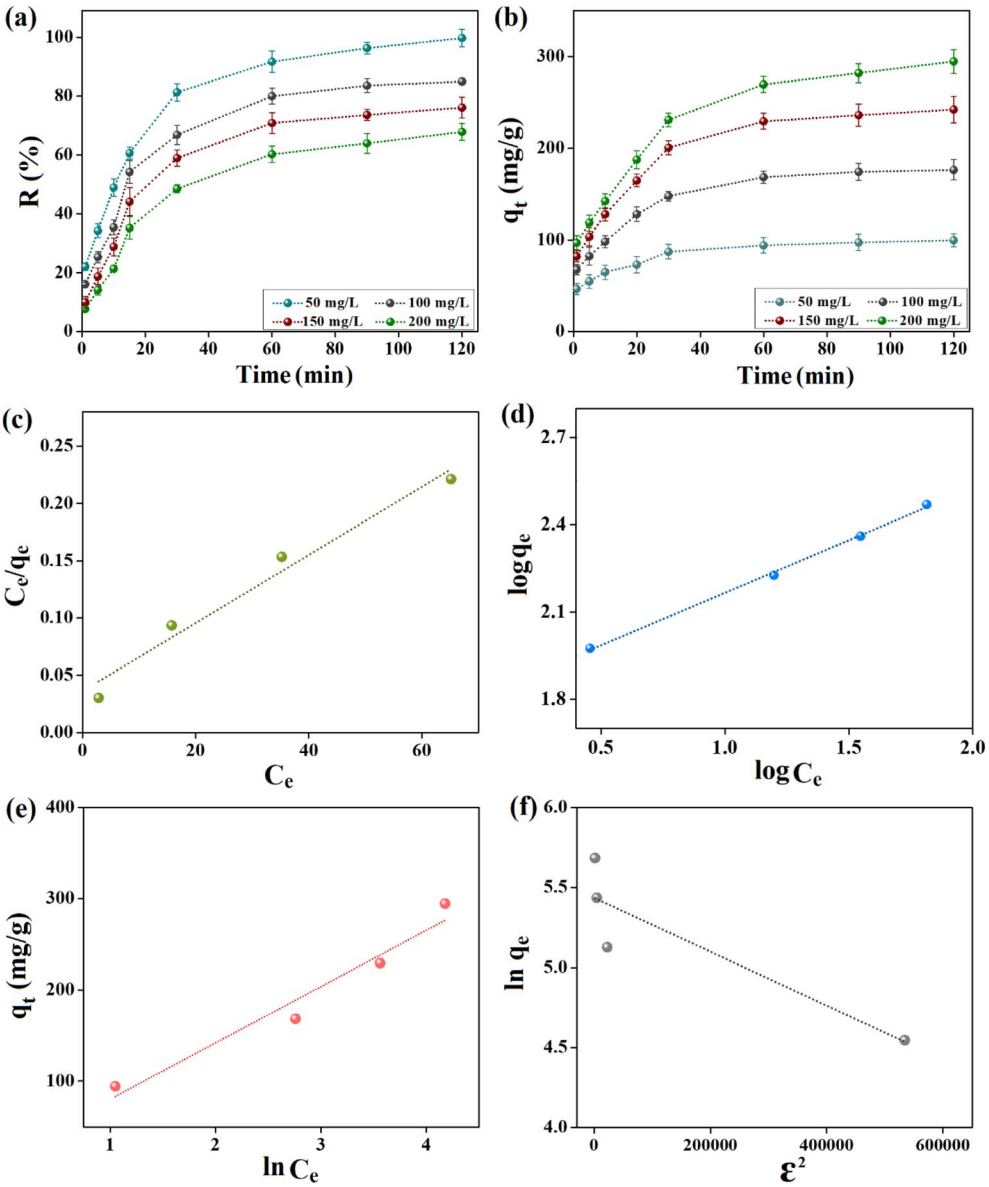

Fig. 5 Effect of increasing the *o*-NP concentration: (a) *R*% *vs.* time and (b) q_t *vs.* time (C_o = 50–200 mg L^{-1}, m = 10 mg, V = 20 mL, T = 20 °C, and pH = 5). Isotherm analysis of the adsorption reaction of *o*-NP onto POPA@A-$BC_{0.5}$ using (c) Langmuir, (d) Freundlich, (e) Temkin, and (f) DR models.

Table 1 Parameters of the Langmuir, Freundlich, Temkin, and DR isotherms for the adsorption of *o*-NP by POPA@A-$BC_{0.5}$

Isotherm model	Parameters	Value
Langmuir	q_{max} (mg g^{-1})	333.33
	K_L (L mg^{-1})	0.083
	R^2	0.973
Freundlich	n	2.76
	K_F ((mg g^{-1}) (L $mg^{-1})^{1/n}$)	63.63
	R^2	0.998
Temkin	k_T (L mg^{-1})	1.35
	b_T (kJ mol^{-1})	39.46
	R^2	0.957
D–R	q_s (mg g^{-1})	229.43
	K_{DR} (mol^2 J^{-2})	2.00×10^{-6}
	E (kJ mol^{-1})	0.500
	R^2	0.810

The isotherm analyses were performed on the equilibrium data of the adsorption reaction of *o*-NP onto the POPA@A-$BC_{0.5}$ composite using Langmuir, DR, Freundlich, and Temkin models (Table S1). Fig. 5c–f illustrates the isotherm plots of the *o*-NP adsorption onto the POPA@A-$BC_{0.5}$ surface. The R^2 values of the isotherm plots (Table 1) clarified the fitting of the Freundlich and Langmuir models to the adsorption reaction of *o*-NP molecules, indicating the contribution of physical and chemical mechanisms to the adsorption of *o*-NP onto POPA@A-$BC_{0.5}$. Furthermore, the Freundlich parameter ($n = 2.76$) indicated the favorable adsorption of *o*-NP onto POPA@A-$BC_{0.5}$.[29,33] Langmuir findings demonstrated the excellent affinity of the POPA@A-$BC_{0.5}$ composite for adsorbing *o*-NP, with a q_{max} of 333.33 mg g^{-1}. From the Temkin isotherm analysis, it was proposed that the heat of *o*-NP adsorption declined linearly with surface coverage owing to the possible interactions between *o*-NP and POPA@A-$BC_{0.5}$. Additionally, the b_T constant was lower than 80 kJ mol^{-1}, which suggested the physisorption of *o*-NP onto POPA@A-$BC_{0.5}$. This finding was consistent with the parameters derived from the DR model, which showed that the mean adsorption energy was below 8 kJ mol^{-1}.

Fig. 6a–c shows the plots of the pseudo-first-order, pseudo-second-order, and Elovich models for the adsorption reaction of *o*-NP onto POPA@A-$BC_{0.5}$. The pseudo-second-order model fit the *o*-NP adsorption onto POPA@A-$BC_{0.5}$ because the R^2 values across all concentrations were higher than those of the pseudo-first-order model, as summarized in Table 2. In addition, the actual equilibrium adsorption capacities for *o*-NP of POPA@A-$BC_{0.5}$ matched the calculated values from the pseudo-second-order model.[34,35] Notably, there was a decrease in K_2 with an increase in the *o*-NP concentration, which implied a competition for the active sites of POPA@A-$BC_{0.5}$ at higher *o*-NP loadings. For the Elovich model, the lower R^2 values denoted a poorer statistical fit to the *o*-NP adsorption reaction onto POPA@A-$BC_{0.5}$. In addition, the high α values confirmed the fast adsorption reaction of *o*-NP, while the decrease in β with increasing *o*-NP concentration implied progressive surface coverage and heterogeneity.

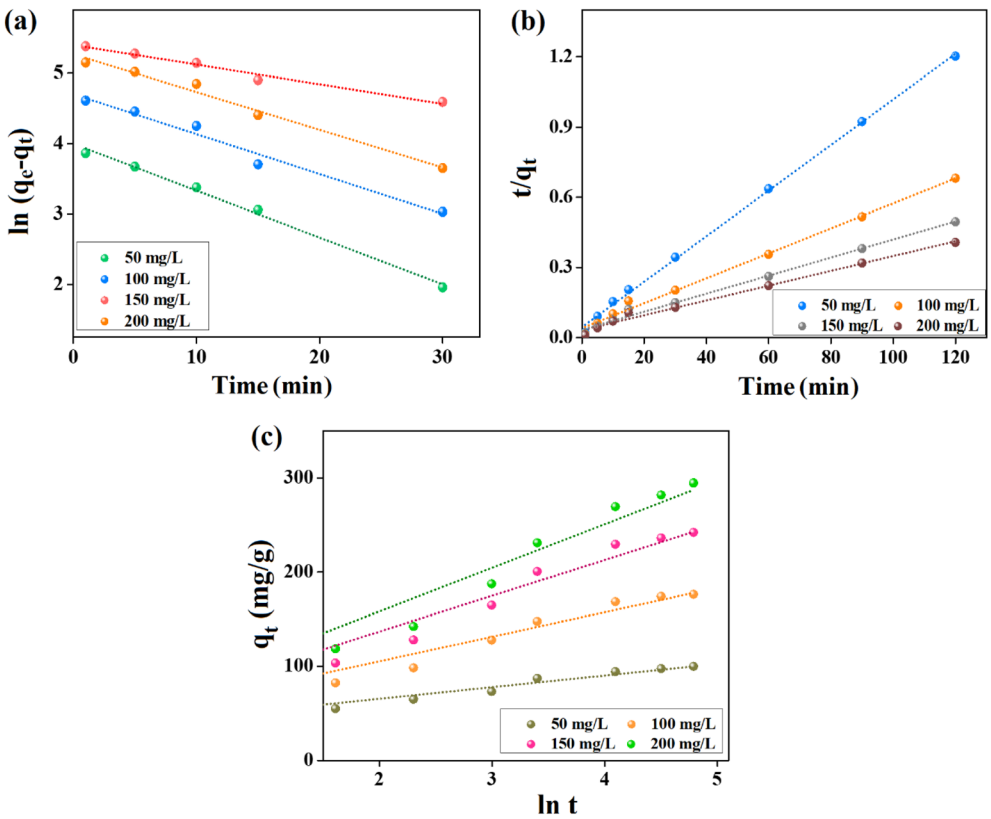

Fig. 6 Kinetic analysis of the adsorption of *o*-NP onto POPA@A-$BC_{0.5}$ using (a) pseudo-first-order, (b) pseudo-second-order, and (c) Elovich models.

Table 2 Pseudo-first-order, pseudo-second-order, and Elovich model parameters for the adsorption of *o*-NP by POPA@A-$BC_{0.5}$

	Concentration (mg L^{-1})			
Kinetic models and their parameters	50	100	150	200
$q_{e,\ Exp}$ (mg g^{-1})	94.29	168.47	229.52	269.63
Pseudo-first-order				
$q_{e,\ Cal}$ (mg g^{-1})	54.53	113.53	197.55	224.60
k_1 (min^{-1})	0.066	0.045	0.044	0.043
R^2	0.997	0.995	0.991	0.992
Pseudo-second-order				
$q_{e,\ Cal}$ (mg g^{-1})	103.09	185.19	256.41	312.50
k_2 (g mg^{-1} min^{-1})	2.09×10^{-3}	8.35×10^{-4}	5.17×10^{-4}	3.53×10^{-4}
R^2	0.999	0.997	0.996	0.994
Elovich				
α (mg g^{-1} min^{-1})	333.57	199.66	187.09	192.06
β (g mg^{-1})	8.1×10^{-2}	3.8×10^{-2}	2.6×10^{-2}	2.2 × 10–2
R^2	0.953	0.944	0.942	0.929

3.4. Mechanistic investigation of *o*-NP

To determine the possible mechanistic pathways of the adsorption of *o*-NP onto POPA@A-$BC_{0.5}$, the XPS spectra of the composite before and after the adsorption reaction were analyzed. The wide spectrum of the used POPA@A-$BC_{0.5}$ (Fig. 7a) revealed an increase in the atomic percentage of N 1s from 4.99% to 6.62%, confirming the *o*-NP adsorption onto the composite surface. The interactions between *o*-NP and POPA@A-$BC_{0.5}$ were suggested as follows:

3.4.1. Electron donor–acceptor interactions. The electron donor–acceptor interaction is a possible mechanism for

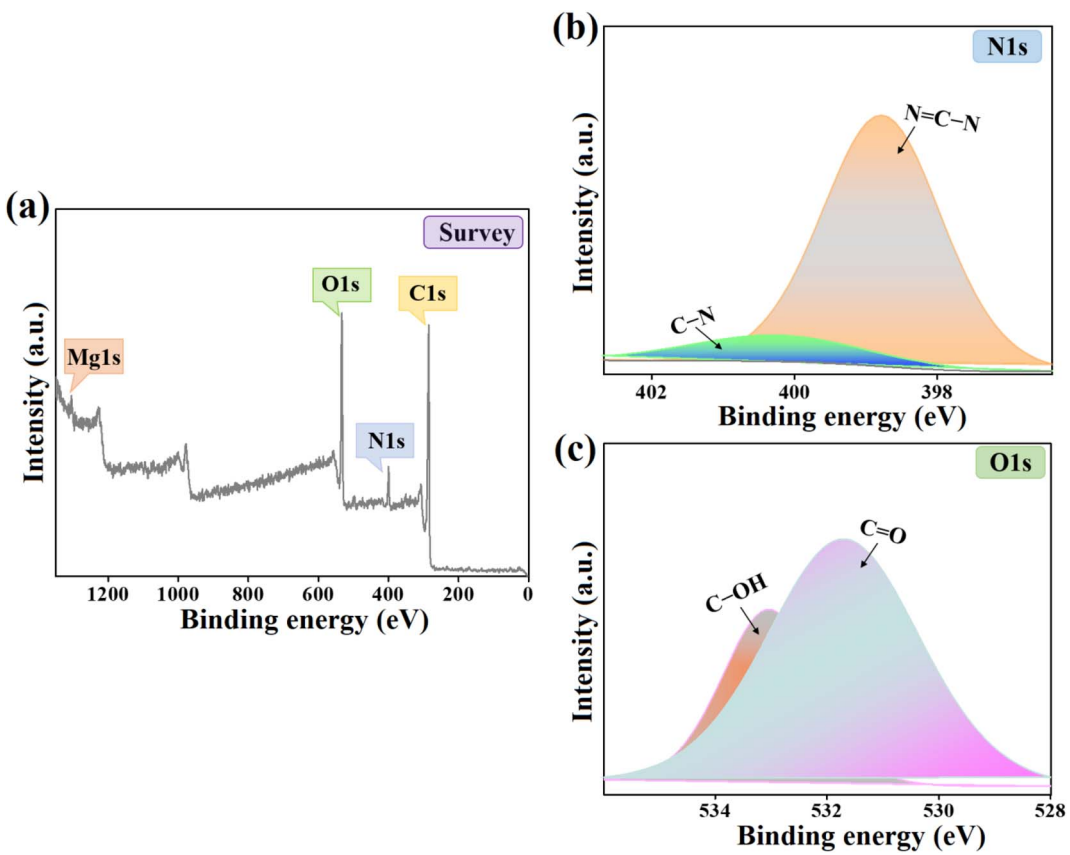

Fig. 7 XPS spectra of the *o*-NP-adsorbed POPA@A-$BC_{0.5}$ composite: (a) wide scan, (b) N 1s, and (c) O 1s spectra.

adsorbing *o*-NP because it possesses a nitro group with a strong electron-withdrawing character and a hydroxyl that serves as an electron donor group. Notably, the POPA@A-$BC_{0.5}$ composite contains many electron donor groups, such as hydroxyl, phenoxy, oxadiazole, and carboxyl. Therefore, *o*-NP can bond with POPA@A-$BC_{0.5}$ *via* electron donor–acceptor interactions. The XPS spectrum of N 1s of *o*-NP-adsorbed POPA@A-$BC_{0.5}$ reveals changes in the peak positions from 398.83 and 400.21 eV to 398.77 and 400.35 eV, respectively, as shown in Fig. 7b. In addition, the peaks of O 1s (Fig. 7c) shift slightly from 533.05 and 531.34 eV to 533.03 and 531.70 eV after the *o*-NP adsorption, respectively. These observations confirm the contributions of oxygen- and nitrogen-containing groups of POPA@A-$BC_{0.5}$ in adsorbing *o*-NP.

3.4.2. Hydrogen bonding. Hydrogen bonding plays a fundamental role in adsorbing the *o*-NP molecule, which comprises a nitro group that acts as a hydrogen acceptor and a hydroxyl group that serves as a hydrogen donor. Meanwhile, the POPA@A-$BC_{0.5}$ composite contains hydroxyl and carbonyl groups, which can act as hydrogen donors and acceptors, respectively. Furthermore, the oxadiazole of POPA@A-$BC_{0.5}$ acts as a hydrogen acceptor, and the phenoxy serves as a hydrogen donor. Consequently, *o*-NP can interact with POPA@A-$BC_{0.5}$ *via* hydrogen bonding between the oxygen of the nitro group of *o*-NP (hydrogen acceptor) and the hydrogen of the hydroxyl, phenoxy, and carbonyl groups of the composite (hydrogen donor), as shown in Fig. 8. Additionally, the oxygen of the hydroxyl group of *o*-NP (hydrogen donor) can form hydrogen bonding with the hydrogen of the hydroxyl, oxadiazole, and carbonyl groups of the composite (hydrogen acceptor).

3.4.3. n → π* interactions and π–π stacking. *o*-NP has electron-deficient aromatic and nitro-group π* orbitals that can act as π-acceptors. Meanwhile, the POPA@A-$BC_{0.5}$ composite possesses electron donor groups, like hydroxyl, phenoxy, and carbonyl. Therefore, the *o*-NP molecules can attach to the adsorption groups of the POPA@A-$BC_{0.5}$ composite *via* n → π* interactions. Moreover, the matrix of POPA@A-$BC_{0.5}$ contains benzene rings that can bond with the benzene ring of *o*-NP molecules *via* π–π stacking.

3.5. Comparative study

There are limited published studies on the removal of *o*-NP, whether by catalysis or adsorption, even though it poses a serious risk to human health and the environment. In addition, there is no previous research addressing the removal of *o*-NP by A-BC or POPA. The adsorption performance of POPA@A-$BC_{0.5}$ toward *o*-NP was compared with that of previously reported adsorbents by considering the adsorption parameters listed in Table 3, including pH, temperature, equilibrium time, reusability, and adsorption capacity. Obviously, the POPA@A-$BC_{0.5}$ composite exhibits an excellent adsorption capacity toward *o*-NP in a short equilibrium time. This promising

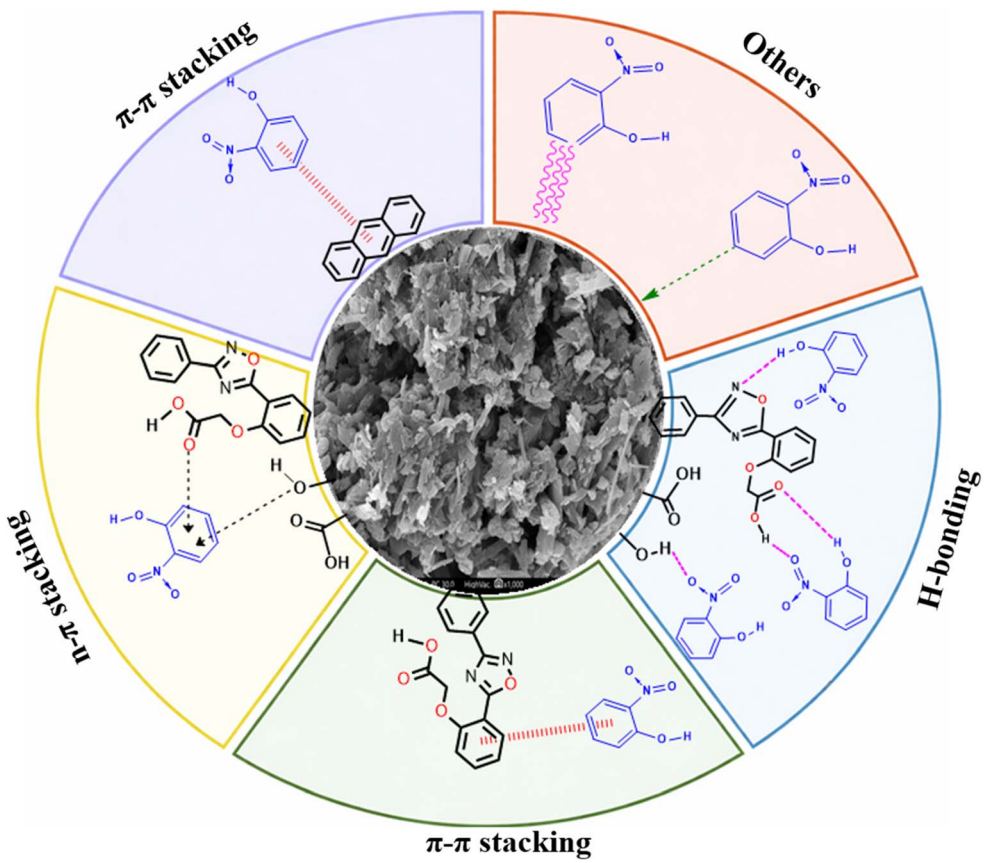

Fig. 8 Schematic of the adsorption mechanisms of *o*-NP onto the POPA@A-$BC_{0.5}$ composite.

Table 3 Comparison of the adsorption performances of the POPA@A-$BC_{0.5}$ composite and previously reported adsorbents toward *o*-NP

Adsorbents	pH	Temp. (°C)	Eq. time (min)	Reusability cycles	q_{max} (mg g^{-1})	Ref.
Kaol/SLS-$BC_{0.5}$/β-$CD_{0.5}$	3	20	90	6	588.24	16
WH-AC	—	28	180	—	47.62	36
Magnetic APcoke/NCs	6	25	100	5	291.55	10
SM CLI-PPHF	2–6	—	1080	3	1.51	37
Fe_3O_4-κ-Carr/MIL-125	6	25	60	5	320.26	38
ACWC-AC	3	25	300	—	179.10	39
POPA@A-$BC_{0.5}$	5	20	60	7	333.33	This study

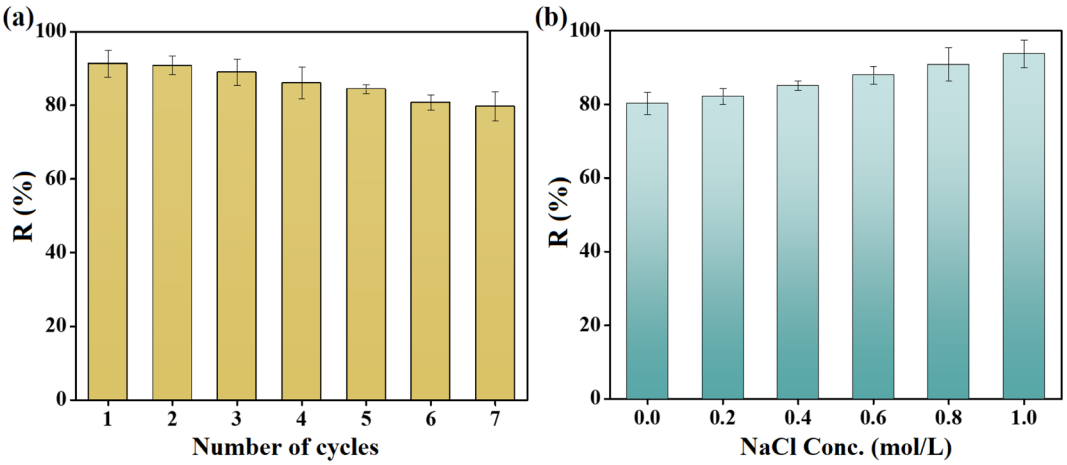

Fig. 9 (a) Reusability of the POPA@A-$BC_{0.5}$ composite for seven *o*-NP adsorption/desorption cycles (C_o = 50 mg L^{-1}, *m* = 10 mg, V = 20 mL, *T* = 20 °C, and pH = 5) and (b) impact of the ionic strength on the *o*-NP adsorption onto the POPA@A-$BC_{0.5}$ composite (C_o = 100 mg L^{-1}, [NaCl] = 0.2–1.0 mol L^{-1}, *m* = 10 mg, V = 20 mL, *T* = 20 °C, and pH = 5).

adsorption capacity of POPA@A-$BC_{0.5}$ toward *o*-NP can be attributed to the abundance of the active groups on the composite surface, which can adsorb *o*-NP *via* many adsorption mechanisms. The POPA@A-$BC_{0.5}$ possesses electron donor groups, like hydroxyl, phenoxy, and carbonyl, which can attack *o*-NP in its solution *via* electron donor–acceptor and n → π* interactions. In addition, the benzene rings in the matrix of POPA@A-$BC_{0.5}$ induce π–π stacking between the composite and *o*-NP. The POPA@A-$BC_{0.5}$ composite has hydrogen donors and acceptors that enable it to form H-bonding with *o*-NP.

3.6. Recyclability study

Fig. 9a demonstrates the reusability of the POPA@A-$BC_{0.5}$ composite during seven *o*-NP adsorption/desorption cycles. The POPA@A-$BC_{0.5}$ composite was collected after each cycle of *o*-NP adsorption and rinsed with NaOH (20 mL, 1 M) to desorb the *o*-NP molecules on the surface of the composite. Notably, the adsorbability of POPA@A-$BC_{0.5}$ slightly declined, retaining an *o*-NP removal percentage of about 80% after the seventh cycle. This decrease in the removal capacity of POPA@A-$BC_{0.5}$ can be attributed to more than one reason: the first one is the loss of mass of the composite during the regeneration step. The second reason for the decline in the *o*-NP adsorption percentage after seven cycles is most likely the strong interactions between POPA@A-$BC_{0.5}$ and *o*-NP, which prevent the desorption of *o*-NP from the binding sites on the surface and interior pores of the composite.

3.7. Ionic strength

The impact of ionic strength on the efficiency of adsorbing *o*-NP using NaCl as an electrolyte was investigated, as shown in Fig. 9b. Surprisingly, the removal percentage of *o*-NP increased from 80.26% to 93.82% after increasing the concentration of NaCl to 1.0 mol L^{-1}. This observation could be explained by the phenomenon of the salting-out effect, in which the presence of NaCl in the adsorption system decreases the solubility of *o*-NP molecules.[40] As a result, it is suggested that the transfer of *o*-NP molecules from the aqueous phase to the POPA@A-$BC_{0.5}$ surface may be promoted because of the decrease in the *o*-NP solubility, thereby enhancing the efficiency of the adsorption process.

4. Conclusion

In conclusion, the POPA@A-$BC_{0.5}$ composite exhibited improved adsorption performance in the adsorption reaction of *o*-NP, where the adsorption percentage attained was 99.69% at 20 °C and pH 5 using 10 mg of POPA@A-$BC_{0.5}$. The SEM image of the POPA@A-$BC_{0.5}$ composite confirmed the presence of POPA crystals on the surface and pores of the A-BC framework. In addition, the zeta potential analysis of the POPA@A-$BC_{0.5}$

composite indicated that the pH_{pzc} was 3.63, confirming that the Coulombic attraction force was not involved in the *o*-NP adsorption pathways. Equilibrium data analysis indicated the participation of both physical and chemical adsorption mechanisms in the removal reaction of *o*-NP by POPA@A-$BC_{0.5}$, and the Freundlich and Langmuir models fitted the reaction. Furthermore, the pseudo-second-order model best fitted the experimental data of the *o*-NP adsorption reaction. Notably, the mechanistic investigation suggested that the *o*-NP adsorption occurred *via* π–π stacking, hydrogen bonds, electron donor–acceptor interactions, and n → π* interactions. Nevertheless, the separation of the POPA@A-$BC_{0.5}$ adsorbent using the conventional centrifugation method was time-consuming. Therefore, improving its separation by decorating POPA@A-$BC_{0.5}$ with a magnetic substance with a strong magnetic character, such as magnetite, may be a useful approach. In addition, formulating POPA@A-$BC_{0.5}$ in a bead or membrane form could be another viable solution to facilitate its separation from the adsorption system. Despite some practical limitations associated with large-scale implementation, the promising results of the present study encourage further investigation of this adsorbent under practical conditions, especially for large-scale applications and the treatment of real wastewater. Future studies may also focus on evaluating the performance of the prepared adsorbent in continuous systems, the presence of coexisting contaminants, and more complex wastewater matrices to further support its practical applicability.

Conflicts of interest

There are no conflicts to declare.

Data availability

The datasets supporting the findings of this study are available within the article and its supplementary information (SI) files. Supplementary information is available. See DOI: https://doi.org/10.1039/d6ra01348a.

Funding

This work was supported by "the Deanship of Scientific Research, Vice Presidency for Graduate Studies and Scientific Research, King Faisal University, Saudi Arabia [Project No. KFU261293]".

Acknowledgements

FMA and MSA acknowledge "the Deanship of Scientific Research, Vice Presidency for Graduate Studies and Scientific Research, King Faisal University, Saudi Arabia, for financial support under the annual funding track [KFU261293]".

References

1 M. Xiao, *et al.*, Recent Progress in covalent organic framework-based membranes: design, synthesis, and applications in the fields of energy and the environment, *ACS Macro Lett.*, 2025, **14**(8), 1201–1220.
2 X. Wang, *et al.*, Recent advances of bifunctional electrocatalysts and electrolyzers for overall seawater splitting, *J. Mater. Chem. A*, 2024, **12**(2), 634–656.
3 M. S. Ayoup, *et al.*, Zwitterionic MOF-embedded alginate beads with polydopamine surface functionalization for efficient doxycycline removal: optimization and mechanistic study, *Int. J. Biol. Macromol.*, 2024, **281**, 136288.
4 R. Agarwala and L. Mulky, Adsorption of dyes from wastewater: A comprehensive review, *ChemBioEng Rev.*, 2023, **10**(3), 326–335.
5 B. S. Marques, *et al.*, Ca–Al, Ni–Al and Zn–Al LDH powders as efficient materials to treat synthetic effluents containing o-nitrophenol, *J. Alloys Compd.*, 2020, **838**, 155628.
6 L. Tabana, *et al.*, Adsorption of phenol from wastewater using calcined magnesium-zinc-aluminium layered double hydroxide clay, *Sustainability*, 2020, **12**(10), 4273.
7 R. Arasteh, *et al.*, Adsorption of 2-nitrophenol by multi-wall carbon nanotubes from aqueous solutions, *Appl. Surf. Sci.*, 2010, **256**(14), 4447–4455.
8 U. EPA, *Ambient Water Quality Criteria for Nitrophenols*. US Environmental Protection Agency, 1980.
9 M. Aazza, *et al.*, Ortho-Nitro-Phenol adsorption onto alumina and surfactant modified alumina: kinetic, isotherm and mechanism, *J. Environ. Chem. Eng.*, 2017, **5**(4), 3418–3428.
10 A. M. Omer, *et al.*, Sustainable synthesis of magnetic petroleum coke/nonanyl chitosan composite for efficient removal of o-nitrophenol, *Sci. Rep.*, 2024, **14**(1), 14463.
11 A. S. Eltaweil, *et al.*, Highly efficient removal of o-nitrophenol by a green Ag@ ZnFe 2 O 4/BC catalyst via Fenton-like oxidation, *RSC Adv.*, 2025, **15**(40), 33549–33560.
12 A. S. Eltaweil, *et al.*, Photocatalytic removal of o-Nitro phenol using phyto-assisted synthesized NiO/CdS@ g-GO catalyst, *J. Solid State Chem.*, 2025, **343**, 125159.
13 X. Zhou, *et al.*, A luminescent Cd-MOF used as a chemosensor for high-efficiency sensing of Fe3+, Cr (IV), trinitrophenol, and colchicine, *ACS Omega*, 2024, **9**(10), 11339–11346.
14 M. S. Ayoup, *et al.*, Antioxidant evaluation of novel 3-Aryl-5-phenyloxy-1, 2, 4-oxadiazoles as radical scavengers: Synthesis, characterization, and ADME studies, *Results Chem.*, 2025, 102508.
15 R. Deng, *et al.*, Biochar-mediated Fenton-like reaction for the degradation of sulfamethazine: role of environmentally persistent free radicals, *Chemosphere*, 2020, **255**, 126975.
16 A. S. Eltaweil, *et al.*, Engineering of a kaolin/SLS-functionalized biochar@ β-cyclodextrin composite for adsorption of o-nitrophenol; optimization, mechanistic study, and Box–Behnken design, *RSC Adv.*, 2026, **16**(2), 1697–1713.
17 S. M. Shaheen, *et al.*, Wood-based biochar for the removal of potentially toxic elements in water and wastewater: a critical review, *Int. Mater. Rev.*, 2019, **64**(4), 216–247.
18 J. Maroušek, *et al.*, Modified biochars present an economic challenge to phosphate management in wastewater treatment plants, *J. Clean. Prod.*, 2020, **272**, 123015.

19 G. Prasannamedha, *et al.*, Enhanced adsorptive removal of sulfamethoxazole from water using biochar derived from hydrothermal carbonization of sugarcane bagasse, *J. Hazard. Mater.*, 2021, **407**, 124825.
20 Z. Luo, *et al.*, Novel insights into the adsorption of organic contaminants by biochar: A review, *Chemosphere*, 2022, **287**, 132113.
21 Y. Wang, *et al.*, Research status, trends, and mechanisms of biochar adsorption for wastewater treatment: a scientometric review, *Environ. Sci. Eur.*, 2024, **36**(1), 25.
22 A. S. Eltaweil, *et al.*, Engineering a sustainable cadmium sulfide/polyethyleneimine-functionalized biochar/chitosan composite for effective chromium adsorption: optimization, co-interfering anions, and mechanisms, *RSC Adv.*, 2024, **14**(31), 22266–22279.
23 C.-Y. Shi, W.-Y. Qin and D.-H. Qu, Semi-crystalline polymers with supramolecular synergistic interactions: from mechanical toughening to dynamic smart materials, *Chem. Sci.*, 2024, **15**(22), 8295–8310.
24 S. Zhang and J. Wang, Removal of chlortetracycline from water by immobilized Bacillus subtilis on honeysuckle residue–derived biochar, *Water, Air, Soil Pollut.*, 2021, **232**(6), 236.
25 S. Yousefi, B. Ghasemi and M. P. Nikolova, Opto-structural characterization of Mg (OH) 2 and MgO nanostructures synthesized through a template-free sonochemical method, *Appl. Phys. A*, 2021, **127**(7), 549.
26 D. Render, *et al.*, Biomaterial-Derived Calcium Carbonate Nanoparticles for Enteric Drug Delivery, *J. Nanomater.*, 2016, **2016**(1), 3170248.
27 J. Wu, *et al.*, Structure–activity relationship of an A-site-doped LaNiO3/SiO2 catalyst, *J. Chem. Res.*, 2022, **46**(2), 17475198211055091.
28 M. Aazza, *et al.*, Performance of first derivative UV/Visible spectra for kinetic and isothermal study of simultaneous adsorption of o-nitrophenol and p-nitrophenol onto Al2O3 and HDTMA+/Al2O3 composite, *J. Mol. Liq.*, 2023, **383**, 122139.
29 S. T. Al-Asadi, *et al.*, Adsorption of methylene blue dye from aqueous solution using low-cost adsorbent: kinetic, isotherm adsorption, and thermodynamic studies, *Environ. Monit. Assess.*, 2023, **195**(6), 676.
30 H. Wang, *et al.*, Discovery of Novel N-[(dimethylamino) methylene] thiourea (TUFA)-Functionalized Lignin for Efficient Cr (VI) Removal from Wastewater, *Toxics*, 2025, **13**(9), 759.
31 A. H. Jawad, *et al.*, Carbonization of corn (Zea mays) cob agricultural residue by one-step activation with sulfuric acid for methylene blue adsorption, *Desalination Water Treat.*, 2018, **118**, 342–351.
32 Y. Zhan, *et al.*, Mussel-inspired polydopamine decorated pomelo peel as a durable biosorbent for adsorption of cationic dyes, *Cellulose*, 2021, **28**(1), 453–470.
33 Z. Bu, *et al.*, Study on the adsorption properties of organically modified diatomite for methylene blue, *Sci. Rep.*, 2025, **15**(1), 27561.
34 Y. Guo, *et al.*, Removal of mercury (II) and methylene blue from a wastewater environment with magnetic graphene oxide: adsorption kinetics, isotherms and mechanism, *RSC Adv.*, 2016, **6**(86), 82523–82536.
35 N. Fayoud, *et al.*, Kinetic, isotherm and thermodynamic studies of the adsorption of methylene blue dye onto agro-based cellulosic materials, *Desalination Water Treat.*, 2016, **57**(35), 16611–16625.
36 T. O. Isichei and F. E. Okieimen, Adsorption of 2-nitrophenol onto water hyacinth activated carbon-kinetics and equilibrium studies, *Environ. Pollut.*, 2014, **3**(4), 99.
37 M. M. Motsa, *et al.*, Adsorption of 2, 4, 6-trichlorophenol and ortho-nitrophenol from aqueous media using surfactant-modified clinoptilolite–polypropylene hollow fibre composites, *Water, Air, Soil Pollut.*, 2012, **223**(4), 1555–1569.
38 E. M. Abd El-Monaem, *et al.*, Adsorption of nitrophenol onto a novel Fe3O4-κ-carrageenan/MIL-125 (Ti) composite: process optimization, isotherms, kinetics, and mechanism, *Environ. Sci. Pollut. Res.*, 2023, **30**(17), 49301–49313.
39 L. Sellaoui, *et al.*, Adsorption of ketoprofen and 2-nitrophenol on activated carbon prepared from winery wastes: a combined experimental and theoretical study, *J. Mol. Liq.*, 2021, **333**, 115906.
40 K. Mukherjee, *et al.*, Adsorption enhancement of methylene blue dye at kaolinite clay–water interface influenced by electrolyte solutions, *RSC Adv.*, 2015, **5**(39), 30654–30659.